

AdaTreeFormer: Few Shot Domain Adaptation for Tree Counting from a Single High-Resolution Image

Hamed Amini Amirkolaei^{1,2}, Miaojing Shi^{*1}, Lianghua He¹, and Mark Mulligan³

¹College of Electronic and Information Engineering, Tongji University, Shanghai, China

²Department of Informatics, King’s College London, London, U.K.

³Department of Geography, King’s College London, London, U.K.

February 6, 2024

Abstract

The process of estimating and counting tree density using only a single aerial or satellite image is a difficult task in the fields of photogrammetry and remote sensing. However, it plays a crucial role in the management of forests. The huge variety of trees in varied topography severely hinders tree counting models to perform well. The purpose of this paper is to propose a framework that is learnt from the source domain with sufficient labeled trees and is adapted to the target domain with only a limited number of labeled trees. Our method, termed as AdaTreeFormer, contains one shared encoder with a hierarchical feature extraction scheme to extract robust features from the source and target domains. It also consists of three subnets: two for extracting self-domain attention maps from source and target domains respectively and one for extracting cross-domain attention maps. For the latter, an attention-to-adapt mechanism is introduced to distill relevant information from different domains while generating tree density maps; a hierarchical cross-domain feature alignment scheme is proposed that progressively aligns the features from the source and target domains. We also adopt adversarial learning into the framework to further reduce the gap between source and target domains. Our AdaTreeFormer is evaluated on six designed domain adaptation tasks using three tree counting datasets, *i.e.* Jiangsu, Yosemite, and London; and outperforms the state of the art methods significantly.

Keywords: Tree counting, few-shot domain adaptation, attention-to-adapt, transformer, remote sensing

1 Introduction

Tree counting and mapping individual trees plays an important role in various applications such as forest management (Ong and Ellison (2021)), urban planning (Eisenman et al. (2019)), environmental monitoring (Johnson et al. (2018)), and ecological balance maintaining (Hennigar et al. (2008)). Counting the number of trees manually is time-consuming, costly, and often results in subjective estimates. Hence, there is a growing demand for the development of fast and accurate tree counting methods from remote sensing images using advanced computer vision algorithms (Ammar et al. (2021)). However, accurately counting trees of different types, sizes, and shapes can be a difficult task due to factors such as varying topography, lighting conditions, and shadows (Yao et al. (2021); Liu et al. (2021a)). These difficulties increase when the aim is to count trees solely from a single aerial image without a 3D digital surface model (DSM). DSM generation using light detection and ranging (LiDAR) or aerial images needs expensive equipment and lengthy data processing (Ghanbari Parmehr and Amati (2021); Liu et al. (2013)), hence making it valuable to develop an algorithm for tree counting without relying on DSM data.

Deep learning has revolutionized the fields of photogrammetry and remote sensing by automating analysis, improving accuracy, and advancing applications such as land cover segmentation and object detection (LeCun et al. (2015), Zhu et al. (2017b), van Soesbergen et al. (2022)). Despite the significant achievements of deep neural networks (DNNs), improving their performance generally depends on the availability of a lot of labeled

*Corresponding author. E-mail: mshi@tongji.edu.cn.

training data, which requires a costly and laborious work for data curation (dos Santos Ferreira et al. (2019)). This challenge intensifies when a DNN encounters multiple distinct domains, where each domain, for instance in tree counting, refers to a specific scenario (urban, countryside, farmland), imagery type (aerial or satellite), with different levels of tree densities, shadows or overlapping among individual trees. Since tree annotation from remote sensing data is notoriously expensive, it is very useful to transfer knowledge from the source domain to the target domain without having to perform many annotations. This leads to a key issue in realistic application: the cross-domain problem, *i.e.* training and test data come from different domains. Previous works on tree counting are mostly implemented as a standard supervised learning problem (Chen and Shang (2022); Weinstein et al. (2019); Ammar et al. (2021); Weinstein et al. (2020); Machefer et al. (2020)) which may suffer from overfitting to varying degrees due to the specific characteristics of the dataset. This is why cross-domain tree counting attracts our attention. Most existing studies on domain adaptation techniques in remote sensing focus on land cover and land use classification (Liu and Li (2014); Tuia et al. (2016)), hyperspectral image classification (Deng et al. (2018)), and scene classification tasks (Song et al. (2019)). A common approach is to use image translation networks such as CycleGAN to translate images from the source domain to the target domain, and then use the translated images to train the network for the considered task (Song et al. (2019); Wang et al. (2019a); Han et al. (2020)). However, it is important to note that the image translation models prioritize high-level features and style transfer (Song et al. (2019); Wang et al. (2019a)), potentially sacrificing fine-grained details like individuals or small objects in the scene (Pang et al. (2021)). This loss of detail can greatly impact the tree counting accuracy.

Our main purpose is to facilitate efficient generalization of tree counting models between two domains. In this respect, we assume that sufficient training data are available in the source domain and that only a limited number of labeled data are available in the target domain, *i.e.* a few-shot domain adaptation problem. The objective is to produce a tree density map for a given input image, depicting the distribution and density of trees in a specific area and providing details about the number of trees per unit area. To obtain accurate tree density maps in the target domain, samples from the source and target domains need to be mapped into a shared feature space to ensure that the projected features are both distinct and domain-invariant. To achieve this, we resort to the transformer model, a prominent deep learning architecture that has suitable potential for domain adaptation in classification and segmentation tasks (Wang et al. (2021a); Dosovitskiy et al. (2020)). Unlike convolutional neural networks (CNNs), which operate on local areas of the image, the transformer models long-range dependencies among visual features throughout the entire image using a global self-attention mechanism. This is realized by dividing the image into non-overlapping patches of a set size and then combining them with positional embeddings through linear embedding (Dosovitskiy et al. (2020)). Nevertheless, how to leverage the ability of the transformer to extract robust cross-domain features for tree counting remains an open question.

To address the above question, we propose an attention-to-adapt mechanism for tree counting based on the transformer in a few-shot domain adaptation setting, which we have named as AdaTreeFormer. The proposed network consists of a transformer-based encoder to convert the input image into a latent representation and a transformer-based decoder with domain adaptation heads to produce the final tree density maps. The AdaTreeFormer has three subnets, namely source, source-target, and target subnets. The encoding parts of these subnets are shared and rely primarily on the self-attention mechanism to extract rich features, as do conventional transformer models. In contrast, we introduce an attention-to-adapt mechanism for decoding: each decoder in the source and target subnets uses a self-domain attention, while the source-target subnet has a cross-domain attention for domain information exchange. This design enables the model to efficiently encode intra-domain dependencies in source and target domains and inter-dependencies between source and target domains while generating tree density maps. Moreover, to ensure effective domain alignment among the output features of the three subnets, we introduce a hierarchical cross-domain feature alignment loss in which the generated self-domain attention maps from the source and target subnets should be close to the generated cross-domain attention maps from the source-target subnet. Last, we adopt an adversarial training approach to further decrease the domain gap and learn domain-invariant feature representations for generating consistently good tree density maps for target images.

Overall, we for the first time propose a few-shot domain adaptation framework for tree counting, incorporating new ideas by leveraging a transformer structure. In summary, we make the following contributions:

- We propose an end-to-end few-shot domain adaptation framework based on transformer architecture for tree counting from a single high-resolution aerial image.
- We propose an attention-to-adapt mechanism that enforces the network to extract relevant information from different domains.
- We introduce a hierarchical cross-domain feature alignment loss to help the network to align the extracted self- and cross-domain attention maps.
- We show that our framework generalizes and adapts to new domains with a much lower average error on the tree counting than state of the art models.

2 Related Work

In this section, we briefly review the relevant works in three subsections: supervised tree counting, cross-domain object counting, and few-shot learning.

2.1 Supervised tree counting

Tree counting in dense forest environments can be challenging due to the close proximity of trees, making it difficult to separate individual trees using traditional image analysis techniques. The recent achievements of DNNs in object recognition tasks (Wang et al. (2019b); Ren et al. (2015)) have motivated scientists to adapt these networks to automatic tree detection and counting. The networks proposed for tree counting can be mainly classified into two groups, namely detection-based and regression-based networks, specified below.

2.1.1 Detection-based methods

Detection-based methods use object detection algorithms to identify and count individual trees. These methods typically use models such as YOLO (Redmon et al. (2016)) and Faster R-CNN (Girshick (2015)), which are pretrained on large image corpus annotated with bounding boxes; next, tree detection models are finetuned on tree-specific datasets using transfer learning (Machefer et al. (2020); Ammar et al. (2021); Weinstein et al. (2019)). Weinstein et al. (2020) have made available an open-access dataset containing tree crown information from several locations across the USA. They develop a delineation technique to generate the required training data for tree counting using LiDAR data. Ammar et al. (2021) conduct a comparative study of four object detection architectures - namely Faster R-CNN, YOLOv3, YOLOv4, and EfficientNet - for accurately counting and locating palm trees from aerial images. Lassalle et al. (2022) present a hybrid approach combining a CNN and watershed segmentation to detect individual tree crowns from remotely sensed images.

2.1.2 Regression-based methods

Instead of trying to localize individual trees by detection, regression-based methods focus on producing a continuous measure of tree density in an image (Chen and Shang (2022); Liu et al. (2021a); Yao et al. (2021)). These methods involve learning a model to produce a density map of the tree distribution in an image, which is then integrated to give an estimate of the total number of trees in the scene. These methods offer several advantages over detection-based methods, particularly in challenging scenarios involving high levels of occlusion and background clutter in densely forested environments. Typically, a Gaussian filter is used to create the density map by calculating a weighted sum of the pixel values around each labeled tree point. Liu et al. (2021a) introduce a pyramidal encoder-decoder network, aiming to handle variations in tree scale distribution by merging information across multiple decoder paths during inference. Similarly, Osco et al. (2020) leverage a CNN to estimate the density map and examine the impact of near-infrared band usage on the prediction quality. Yao et al. (2021) explore the performance of different networks such as VGGNet, AlexNet, and a two-column CNN built on the VGGNet and AlexNet backbones to estimate tree density map. Chen and Shang (2022) have developed a method that incorporates both CNNs and transformer

blocks for tree density map estimation. This architecture enables them to capture the global context while retaining the local information needed to represent tree distribution in complex scenes accurately. Finally, Amini Amirkolaei et al. (2023) propose a semi-supervised tree counting network. It focuses on increasing network performance by exploiting unlabeled images to reduce the need for labeled data. However, the performance of this network is reduced when training and test data belong to different domains.

2.2 Cross-domain object counting

In addition to the above-mentioned supervised tree-counting methods, Zheng et al. (2020) proposes a cross-domain object detector for oil palm tree counting using different satellite images, which uses adversarial learning to exploit the transferability between the source and the target domains. Cross-domain adaptation has been the research subject for other counting tasks. Machefer et al. (2020) have developed a method for counting plants using drone images, which involves deploying a Mask R-CNN model and implementing transfer learning to minimize the need for extensive training data. Wang et al. (2019a) compile a comprehensive synthetic crowd dataset to initially form a model capable of producing improved accuracy on real-world datasets through subsequent fine-tuning. Li et al. (2019) tackle varying object scales and density distributions through adversarial training using multi-scale pyramid patches from both the source and target domains. They achieve consistent object counts across different scales by applying a ranking constraint across the pyramid levels. Reddy et al. (2021) employ a guiding network to extract batch normalization parameters from the unlabeled images of the target domain for crowd counting. Liu et al. (2022b) formulate mutual transformations between regression- and detection-based models as two scene-agnostic transformers. They introduce a self-supervised co-training scheme on the target to finetune the regression and detection models using generated pseudo labels, thereby iteratively enhancing the performance of both. Du et al. (2023) introduce a method for training a model on a single source domain to generalize to unseen domains in crowd counting. They divide the source domain into sub-domains for meta-learning and refine the division dynamically. Additionally, they utilize domain-invariant and domain-specific crowd memory modules to disentangle image features.

2.3 Few-shot Learning

Few-shot learning refers to the capability of a model to perform well on previously unseen tasks when presented with only a small amount of training data. Several approaches have emerged over the years: early methodologies (Bart and Ullman (2005); Fink (2004); Fei-Fei (2006)) use hand-crafted features such as local scale-invariant features to transfer knowledge from shared features and contextual information. While more recent ones, such as the memory-based models (Vinyals et al. (2016)), LSTM-based meta-learning (Ravi and Larochelle (2017); Yang et al. (2024)), prototypical networks (Santoro et al. (2016); Huang et al. (2022)), model-agnostic meta-learning (MAML) (Finn et al. (2017)) are based on learned features that are automatically extracted from DNN models. Vinyals et al. (2016) employ memory components within a neural network to acquire a shared representation from minimal data. Santoro et al. (2016) introduce the prototypical networks that acquire a metric space where classification is achieved by calculating distances to prototype representations of individual classes. Additionally, Ravi and Larochelle (2017) employ an LSTM-based meta-learner to acquire an update rule for training a neural network, facilitating improved adaptation to new tasks with limited data. Finn et al. (2017) utilize a model-agnostic meta-learning (MAML) that learns an optimal model parameter initialization, enabling improved generalization to similar tasks through meta-learning. Santoro et al. (2016) highlight the augmented memory neural network for remembering previous tasks and use it to train a model for new tasks. In parallel, Mishra et al. (2017) introduce a general meta-learning architecture that combines temporal convolutions for aggregating past information with soft attention for focusing on specific details. Liu et al. (2022a) propose sharp-MAML to enhance the performance in few-shot meta-learning by leveraging sharpness-aware minimization.

Although most of the above few-shot learning techniques are used in classification tasks, there is also some research on few-shot object counting, which is mainly used for crowd counting. Hossain et al. (2019) apply MAML for one-shot crowd counting; while Reddy et al. (2020) use MAML for scene adaptive crowd counting. Recently, Wang et al. (2021b) propose a neuron linear transformation method for crowd counting, exploiting

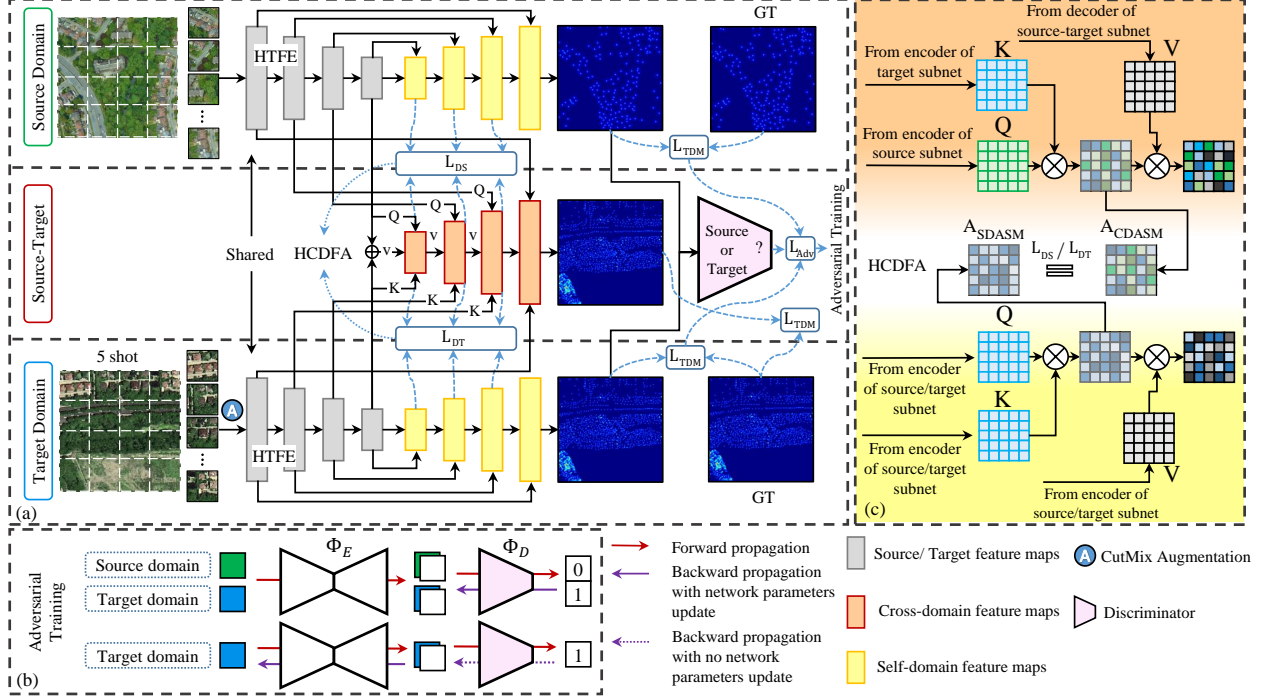


Figure 1: Overview of the proposed AdaTreeFormer framework. (a) In the source domain subnet, the estimated tree density maps of the source domain are optimized with ground truth (GT) using L_{TDM} . The similar pipeline goes to the target domain subnet with the few-shot target domain images, obtained through Cutmix augmentation. The estimated tree density maps in the source-target subnet, produced after the cross-domain attention, are optimized using GT of the target domain through L_{TDM} , while the estimated feature maps are refined using L_{DT} and L_{DS} . An adversarial training is employed that is optimized with L_{Adv} . (b) Explanation of the processes of advised adversarial training in one iteration. (c) The structure of the HC DFA using the self- and cross-domain attention score maps (A_{SDASM} and A_{CDASM}) for a specific scale. When the input feature maps in the lower yellow part are from the source subnet, the equality between A_{SDASM} and A_{CDASM} is equivalent to L_{DS} in $L_{HC DFA}$, and when those feature maps are from the target subnet, this equality is equal to L_{DT} .

domain factor and bias weights to learn the domain shift.

In general, the benefit of conventional tree counting networks lies in their ability to produce accurate tree numbers in a specific domain. It is crucial to provide a domain adaptation method due to the infeasibility of providing training data that covers all different domains.

3 Methodology

3.1 Overview

This paper proposes a few-shot domain adaptation framework to estimate the density map of trees from a single remote sensing image. An overview of the designed framework is presented in Fig. 1. Our framework has a hierarchical tree feature extraction (HTFE) module based on the transformer encoder (Section 3.2.1) that has a shared weight for the source and target domains. Given an image from the source domain ($\mathcal{I}_s \in \mathbb{R}^{H \times W \times 3}$) and another one from the target domain ($\mathcal{I}_t \in \mathbb{R}^{H \times W \times 3}$), the HTFE generates multi-

scale feature maps from them, \mathcal{F}^s and \mathcal{F}^t , respectively. We design a domain adaptive decoder with three subnets: the source, target, and source-target subnets. The source subnet estimates the tree density map corresponding to \mathcal{I}_s as \mathcal{T}_s using \mathcal{F}^s , while the target subnet estimates the tree density map of \mathcal{I}_t as \mathcal{T}_t using \mathcal{F}^t . Additionally, the source-target subnet utilizes \mathcal{F}^s and \mathcal{F}^t to estimate the \mathcal{T}_{st} corresponding to \mathcal{I}_t . An attention-to-adapt mechanism is proposed to help the model learn domain-invariant representations from both domains. This mechanism plays the role of self-domain adaptation in the source and target subnets and cross-domain adaptation in the source-target subnet. By leveraging the self- and cross-domain attention maps, the model learns to adapt to the differences between domains and improve its performance on the target domain (Section 3.2.2). A domain adaptive learning strategy is introduced that contains three parts including supervised learning, cross-domain learning, and adversarial learning. The tree distribution matching (TDM) loss is employed for the supervised learning of all subnets of the proposed framework (Section 3.3.1). We design the hierarchical cross-domain feature alignment (HCDFA) with the objective of aligning the self-domain attention maps with the cross-domain attention score maps (Section 3.3.2). Finally, a domain discriminator network (see pink trapezia in Fig. 1) is employed to determine the domain of the \mathcal{T}_s and \mathcal{T}_t (Section 3.2.3). We employ adversarial learning to make the feature distributions of the source and target subnets close (Section 3.3.3). Overall, throughout the training process all subnets are utilized, while only the target subnet is employed for testing.

3.2 AdaTreeFormer Framework

This section includes two parts, one is the HTFE module that is based on the transformer as the encoder of our AdaTreeFormer. Moreover, we introduce the attention-to-adapt mechanism as the decoder of our model. They are also illustrated in Fig. 2 in detail.

3.2.1 Hierarchical Tree Feature Extraction

We develop the HTFE based on the transformer (Liu et al. (2021b)) to effectively extract multi-scale features during the encoding part of the network (Fig. 2a). In the HTFE, the input image ($H \times W \times 3$) is divided into 4×4 non-overlapping patches, where each patch is considered a token and its feature is formed by concatenating the raw pixel RGB values. Thus, the feature dimension of each patch is $4 \times 4 \times 3 = 48$. In the first scale, a linear embedding layer projects each achieved patch into the dimension of $\frac{H}{4} \times \frac{W}{4} \times 128$. Then, the shifted window transformer block (SWTB) (Fig. 2b) is applied to the patch (Liu et al. (2021b)).

The purpose of the shifted window transformer block (SWTB) (Fig. 2b) is to efficiently capture long-range dependencies in an image by dividing it into shifted windows and applying self-attention within each window. This block is constructed by substituting the conventional multi-head self-attention (MSA) module in a transformer block with a module that relies on shifted windows. In the SWTB, the shifted window-based MSA module is preceded by a 2-layer multilayer perceptron (MLP) with GELU non-linearity in the middle. Each MSA module and MLP are preceded by a layer normalization (LN) and a residual connection is appended after each module, respectively (Liu et al. (2021b)).

In order to create a hierarchical multi-scale representation, the number of tokens is decreased by applying a patch merging layer when the network gets deeper. The initial patch merging layer in the second scale concatenates the feature maps of each group of 2×2 neighboring patches and applies a linear layer to the concatenated feature maps, reducing the number of tokens by a factor of 4 (2×2) and setting the output dimension to 256 (see Fig. 1c). Similarly, the patch merging and SWTB are applied in the third and fourth scales to generate feature maps with the resolution of $\frac{H}{16} \times \frac{W}{16} \times 512$ and $\frac{H}{32} \times \frac{W}{32} \times 1024$, respectively. Following (Liu et al. (2021b)), the encoder comprises 2 layers in the first, second, and fourth scales, while the third scale consists of 18 layers ($\tau \in \{2, 2, 18, 2\}$).

As seen in Fig. 1a, the HTFE is applied to both source and target data for extracting feature maps from them. The source domain contains a large number of labeled images, while the target domain has only a limited number of labeled images available. Therefore, to strengthen the target training data and make the network unbiased, the Cutmix method (Yun et al. (2019)) is used as a data augmentation technique to increase the training data of the target domain. While traditional methods apply transformations independently

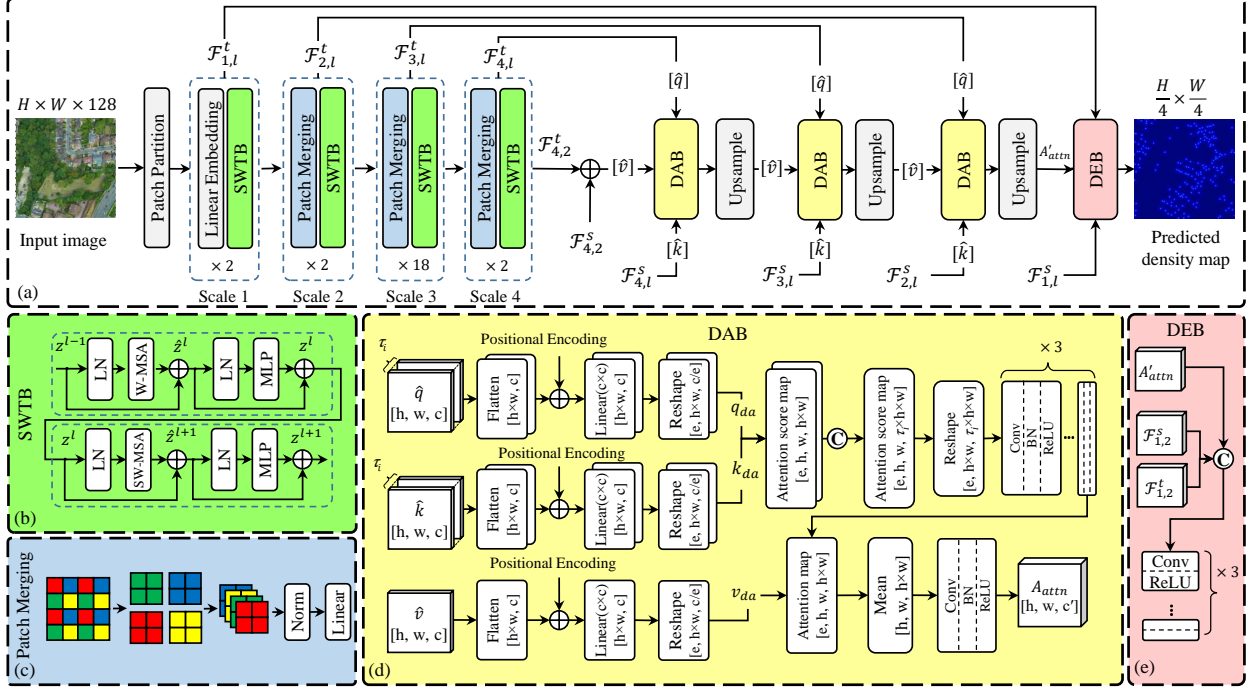


Figure 2: (a) The details of the encoder-decoder part of the proposed AdaTreeFormer. Given the input image, multi-scale features are firstly extracted through the linear embedding, shifted windows transformer block (SWTB), and patch merging module in the encoder. The domain attention blocks (DAB) and density estimation block (DEB) in the decoder align the source and target domains and generate the tree density map, respectively. (b) The structure of the SWTB for extracting feature maps. (c) The patch merging module incorporates information from different image patches into a single unified representation. (d) The DAB generates the self- or cross-domain attention maps using the produced feature maps from the encoder part of the network. (e) The DEB estimates the final tree density map by fusing the generated feature maps from the encoder ($\mathcal{F}_{1,2}^s$ and $\mathcal{F}_{1,2}^t$) and the last layer of the decoder (A_{attn}^l).

to individual images, CutMix combines two random images by cutting out a patch from one image and replacing it with a patch from the other. This creates a new training sample with mixed information that encourages the model to learn more robust and discriminative features by forcing it to rely on different parts of the two images. (Yun et al. (2019)).

3.2.2 Attention-to-Adapt Mechanism

The purpose of the attention-to-adapt mechanism is to help the model to focus on domain-invariant information from different domains while generating tree density maps. The mechanism is implemented across the three subnets of our framework. After passing the source and target images through the encoder, a collection of multi-scale feature maps are generated through HTFE, *i.e.* $\mathcal{F}_{i,l}^s$ and $\mathcal{F}_{i,l}^t$, where i is the scale of the feature maps with respect to the input image, $i \in \{1, 2, 3, 4\}$; l is the index of certain layer of a specific scale, $l \in \{1, \dots, \tau_i\}$; s and t indicate the source and target domains. These feature maps are considered as the input of our proposed attention-to-adapt mechanism. This mechanism comprises two major blocks including domain attention block (DAB) and density estimation block (DEB).

The DAB (Fig. 2d) is to generate self-domain attention maps to ensure efficient encoding of intra-domain dependencies in both the source and target subnets. Additionally, it generates the cross-domain attention maps to account for the inter-dependencies between these domains in the source-target subnet. This block is

based on the transformer (Vaswani et al. (2017)) and employs positional encoding and multi-head attention to compute attention maps.

The DEB (Fig. 2e) serves as the final block responsible for computing the tree density map (Fig. 2a). It achieves this by applying convolutional and Relu layers to the concatenation of A'_{attn} obtained from the preceding layer and $\mathcal{F}_{1,2}^s$ and $\mathcal{F}_{1,2}^t$ from the encoder, employing skip connections.

Domain Attention Block: The DAB is designed to produce the self-/cross-domain attention maps using the generated feature maps through the encoder part of the network. Following the self-attention as the main component of the transformer architecture (Vaswani et al. (2017)), the attention maps are computed as follows:

$$A_{attn}(q_{da}, k_{da}, v_{da}) = softmax\left(\frac{q_{da}k_{da}^T}{\sqrt{d}}\right)v_{da} \quad (1)$$

where q_{da} , k_{da} , and v_{da} represent sets of query, key, and value vectors and d denotes the dimension of the query and key vectors. We adopt this equation to compute dense pixel-wise attention across extracted feature maps from the same or different domains. Therefore, the extracted feature maps from the encoder are specified as \hat{q} , \hat{k} , and \hat{v} . \hat{q} can be from the same/different domains of \hat{k} and \hat{v} . These matrices change depending on whether the aim is to extract self- or cross-domain attention maps. The HTFE generates τ_i layer feature maps for i^{th} scale of the encoder (Section 3.2.1). Hence, the \hat{q} and \hat{k} are multi-layer feature maps according to the τ_i , while \hat{v} initially contains the last-layer feature maps of the fourth scale of the encoder (see Fig. 2d). The dimension of \hat{v} and each layer of \hat{q} , \hat{k} , is equal to $[h \times w \times c]$, where h , w , and c are the height, width, and channel number, respectively. We flatten the \hat{v} and each layer of \hat{q} and \hat{k} into the dimension of $[h \times w, c]$ to treat each pixel as a token and a positional encoding is added to it. Similar to the original transformer (Vaswani et al. (2017)), we employ sine and cosine functions with different frequencies for positional encoding and utilize multi-head attention. After adding the positional encoding, a linear projection ($c \times c$) is applied, and the outcomes of this projection are reshaped according to the number of heads (e) of the multi-head attention to achieve the q_{da} , k_{da} , and v_{da} . The attention score maps are computed using $softmax(q_{da}k_{da}^T/\sqrt{d})$, resulting in a dimension of $[e, h, w, h \times w]$. The resulting multi-layer attention score maps are concatenated together, obtaining attention score maps with the dimension of $[e, h, w, \tau_i \times h \times w]$ (see Fig. 2d). After reshaping the concatenated maps, they are passed through three consecutive series of convolutional, batch normalization, and ReLU layers, and the resulting computation is multiplied by \hat{v} (Eq. 1) to obtain the self- or cross-domain attention maps with a dimension of $[e, h \times w, h \times w]$. Finally, we average the outputs of the multiple heads for each token, pass the tensor through convolutional, batch normalization, and ReLU layers, and obtain $A_{attn} \in R^{h \times w \times c'}$.

Cross-Domain Attention: In order to emphasize the relationships between images originating from distinct domains, we introduce cross-domain attention with an unidirectional scheme from the source to the target domain, focusing on optimizing outcomes within the target domain. First, the last-layer feature maps of the fourth scale from the source ($\mathcal{F}_{4,2}^s$) and target ($\mathcal{F}_{4,2}^t$) domains are added together to generate \hat{v} (Fig. 2a). In addition, we consider the source domain feature maps as \hat{k} and the target domain feature maps as \hat{q} for computing the cross-domain attention maps (Fig. 2a). We perform DAB on feature pairs ($\mathcal{F}_{i,l}^s$ and $\mathcal{F}_{i,l}^t$) for each intermediate layer l of a specific scale i . The output is then upsampled using bilinear interpolation and is used as the \hat{v} of the next DAB, along with $\mathcal{F}_{i+1,l}^s$ and $\mathcal{F}_{i+1,l}^t$ being the new \hat{q} and \hat{k} . This process is repeated each time the DAB is used, for a total of three times, resulting in a collection of intermediate cross-domain attention maps. Finally, after applying the last upsampling layer and achieving the A'_{attn} , the DEB is applied to compute the tree density map (Fig. 2a). Within this DEB, the $\mathcal{F}_{1,2}^s$ and $\mathcal{F}_{1,2}^t$ as the last-layer feature maps of the first scale from the source and target domains are concatenated by a skip connection (Fig. 2e). Subsequently, the combined result in DEB undergoes three consecutive convolutional and ReLU operations to reduce the number of channels to 1 and generate the tree density map. Overall, the cross-domain attention is used in the source-target subnet to estimate the \mathcal{T}_{st} using $\mathcal{F}_{i,l}^s$ and $\mathcal{F}_{i,l}^t$.

Self-Domain Attention: The purpose of computing self-domain attention maps is to focus on relationships between different regions of an image within a domain. The structure of the self-domain attention is similar to the cross-domain attention except that it is computed within one domain by taking the \hat{q} and \hat{k} from the same domain at each scale ($\mathcal{F}_{i,l}^s$ or $\mathcal{F}_{i,l}^t$) instead of two different domains. Utilizing the self-domain attention in the source and target subnets leads to generating the \mathcal{T}_s and \mathcal{T}_t .

3.2.3 Domain Discriminator

In order to further enhance generalizability across different domains, our network is trained using an adversarial approach where an additional tree domain discriminator is involved. The role of the tree domain discriminator is to determine whether an image belongs to the target domain or source domain. Our domain discriminator architecture follows the structure of the classic VGG16 network (Simonyan and Zisserman (2014)) that takes the \mathcal{T}_s and \mathcal{T}_t as input. It consists of 16 layers, including 13 convolutional layers and 3 fully connected layers (Fig. 2g). Each convolutional layer is followed by a ReLU activation function and uses 3×3 filters for convolution. The discriminator also incorporates max pooling layers to reduce the spatial resolution of feature maps. The flattened feature maps are then passed through fully connected layers. A softmax activation function is used in the last layer to assign probabilities to source and target classes. Further elaboration on the loss function is provided in Section 3.3.3.

3.3 Domain Adaptive Learning strategy

The learning strategy consists of three components: tree distribution matching (TDM), cross-domain feature alignment, and adversarial learning. The TDM involves optimizing network parameters by comparing the number of trees present in the estimated density map with the ground truth. The cross-domain feature alignment aligns the source and target domains by ensuring the similarity of the extracted self- and cross-domain attention score maps. Lastly, adversarial learning helps in making the feature distributions of the source and target domains similar.

3.3.1 Tree Distribution Matching

The main idea of the TDM is to treat tree counting as a distribution matching problem (Wang et al. (2020a)). Instead of directly estimating the tree density map, the TDM focuses on matching the distribution of the predicted tree density map with the ground truth distribution. This loss function incorporates a combination of the counting loss (L_{count}), optimal transport loss (L_{ot}), and total variation loss (L_{tv}). The L_{count} measures the absolute difference between the estimated and ground truth tree numbers:

$$L_{count} = \sum_{k=1}^K |||\mathcal{S}_k|| - ||\mathcal{G}_k||| \quad (2)$$

where $\mathcal{S} \in \{\mathcal{T}_s, \mathcal{T}_t, \mathcal{T}_{st}\}$ contains the estimated density maps and $\mathcal{G} \in \{\mathcal{T}_s^{gt}, \mathcal{T}_t^{gt}, \mathcal{T}_t^{gt}\}$ contains their corresponding ground truth map, respectively; $K = 3$ and $||\cdot||$ refers to the L1 norm used to aggregate the density values. The L_{ot} is inspired by the optimal transport theory (Arjovsky et al. (2017)), which is a mathematical approach used to measure the dissimilarity between two different distributions. The L_{ot} Loss compares the distribution of the predicted tree density map with the distribution of the ground truth by considering the optimal transportation plan between the two. The L_{ot} loss is calculated using the optimal transport cost (ψ), as described in (Wang et al. (2020a)):

$$L_{ot} = \sum_{k=1}^K \psi\left(\frac{\mathcal{S}_k}{||\mathcal{S}_k||}, \frac{\mathcal{G}_k}{||\mathcal{G}_k||}\right) \quad (3)$$

The L_{tv} is a measure of the overall variation or complexity of an image by taking the sum of differences between the distribution of the estimated tree density map and the ground truth. This loss is applied to

address the poor approximation of L_{ot} in regions of low density (Wang et al. (2020a)).

$$L_{tv} = \sum_{k=1}^K \frac{1}{2} \left\| \frac{\mathcal{S}_k}{\|\mathcal{S}_k\|} - \frac{\mathcal{G}_k}{\|\mathcal{G}_k\|} \right\| \quad (4)$$

The overall tree distribution (L_{TDM}) matching loss for pixel-level learning is formulated as:

$$L_{TDM} = \phi_1 L_{count} + \phi_2 L_{ot} + \phi_3 L_{tv} \quad (5)$$

where ϕ_1 , ϕ_2 , and ϕ_3 are the weight values that are set to 1, 0.1, and 0.01 according to (Wang et al. (2020a)), respectively.

3.3.2 Hierarchical Cross Domain Feature Alignment

The purpose of the hierarchical cross domain feature alignment (HC DFA) is to boost the robustness of our model’s predictions when tested on previously unseen images by sharing knowledge across domains via feature alignment. A sequential feature alignment at three scales of the decoder is employed to progressively align the source and target sequence features. As shown in Fig. 1a, the proposed framework has three different subnets, in which the self-domain attention score maps (A_{SDASM}) are extracted from the first and last subnets while the cross-domain attention maps (A_{CDASM}) from the middle subnet (see Fig. 1c). The close distance between the self- and cross-domain attention score maps would enforce the model to generate domain-invariant feature maps, agnostic to any specific domain. This introduced loss function ($L_{HC DFA}$) is described as follows:

$$L_{DS} = \sum_{i=2}^4 [A_{CDASM}(i) - A_{SDASM}^s(i)]^2 \quad (6)$$

$$L_{DT} = \sum_{i=2}^4 [A_{CDASM}(i) - A_{SDASM}^t(i)]^2 \quad (7)$$

$$L_{HC DFA} = \beta_1 L_{DS} + \beta_2 L_{DT} \quad (8)$$

where L_{DS} represents the distance between the cross-domain attention score maps ($A_{CDASM}(i)$) and the source domain attention score maps ($A_{SDASM}^s(i)$), while L_{DT} represents the distances between the cross-domain ($A_{CDASM}(i)$) and the target domain ($A_{SDASM}^t(i)$) attention score maps. The attention score maps are obtained following the aforementioned sections (Sec. 3.2.2); i represents the scale of the corresponding encoder feature maps ($i \in \{2, 3, 4\}$) that is used. β_1 and β_2 are the weight values for L_{DS} and L_{DT} respectively. Computing a weighted average of the L_{DT} and L_{DS} is critical to strike a balance between the source and target domains to obtain optimal results.

3.3.3 Adversarial Learning

Referring to Sec. 3.2.3, our framework consists of two parts: the tree density generator (Φ_G), which encompasses the shared encoder with the source and target subnets, and an additional tree domain discriminator network (Φ_D) (Fig. 1b). Φ_G generates tree density maps for input images, while Φ_D determines if an image is from the source or target domain. During the model’s training, we train Φ_G to generate \mathcal{T}_s from \mathcal{I}_s using the source subnet and \mathcal{T}_t from \mathcal{I}_t using the target subnet, employing the supervised loss (L_{TDM}). Meanwhile, we train Φ_D to assign high scores (1) to the \mathcal{T}_s and low scores (0) to the \mathcal{T}_t . Φ_D learns to differentiate between the source and target domain data, while the Φ_G simultaneously aims to produce domain-invariant representations, thereby enhancing the model’s adaptation to the target domain. Given m source domain training images \mathcal{I}_s and n target domain training images \mathcal{I}_t with their corresponding ground truth (\mathcal{T}_s and \mathcal{T}_t), we define the loss function following (Zhang et al. (2017b)):

$$\min_{\theta_{\Phi_G}} \max_{\theta_{\Phi_D}} L_{Adv}(\theta_{\Phi_G}, \theta_{\Phi_D}) = \sum_{i=1}^m L_{TDM}^s + \sum_{i=1}^n L_{TDM}^t - \lambda \left[\sum_{i=1}^m L_{bce}(\Phi_D(\Phi_G(\mathcal{I}_s), \mathcal{I}_s), 1) + \sum_{i=1}^n L_{bce}(\Phi_D(\Phi_G(\mathcal{I}_t), \mathcal{I}_t), 0) \right] \quad (9)$$

where, θ_{Φ_G} and θ_{Φ_D} are the parameters of the Φ_G and Φ_D , respectively. L_{bce} represents the binary-class cross-entropy loss, L_{TDM}^s and L_{TDM}^t represent the computed L_{TDM} for source and target domain images. The terms of $\sum_{i=1}^m L_{TDM}^s + \sum_{i=1}^n L_{TDM}^t$ in the L_{Adv} represent the supervised training of Φ_G using source and target data, while the remained terms represent the adversarial training part. During the training process, we minimize a part of the loss with respect to the parameters θ_{Φ_G} of Φ_G , while maximizing the loss with respect to the parameters θ_{Φ_D} of Φ_D .

3.3.4 Training loss

Overall, the final loss function is composed of three different losses. The first loss is based on the summation of the computed supervised loss (L_{TDM}) of the three subnets of the network including the source (L_{TDM}^s), target (L_{TDM}^t), and source-target (L_{TDM}^{st}) losses ($L_{TDM} = L_{TDM}^s + L_{TDM}^t + L_{TDM}^{st}$). The second and the third losses are the L_{HCDF_A} and L_{Adv} . The final loss is:

$$L = L_{TDM} + L_{HCDF_A} + L_{Adv} \quad (10)$$

3.3.5 Inference

During the inference process, only the target subnet is employed, as depicted in Fig. 1a.

4 Experiments

4.1 Datasets

We employ three different datasets which were gathered from different domains, *i.e.* different countries that contain various tree shapes, sizes, and distributions (Fig. 3).

4.1.1 Jianguo Dataset

This dataset encompasses 24 satellite images taken by the GaofenII satellite with a ground sample distance (GSD) of 0.8m. These images were captured in Jianguo Province, China (Yao et al. (2021); Liu et al. (2021a)), which cover diverse landscapes such as urban residential, cropland, and hills. There are 664,487 manually annotated trees spread across 2400 images, 1920 images are used for training while 480 images for testing.

4.1.2 London Dataset

This dataset consists of high-resolution images captured at 0.2m GSD from London, United Kingdom for training and testing (Amini Amirkolaei et al. (2023)). Among the labeled images, 452 samples are designated for training and 161 samples are for testing. There are 95,067 trees that are manually annotated across 613 images. The images cover different landscapes such as urban residential areas and dense parks. This dataset is divided into a training set of 450 images and a test set of 152 images.

4.1.3 Yosemite Dataset

The study area for this dataset revolves around Yosemite National Park, located in California, United States of America (Chen and Shang (2022)). It comprises a rectangular image from Google Maps with dimensions of $19,200 \times 38,400$ pixels and a GSD of 0.12m. Within this image, 98,949 trees have been manually annotated. The image is split into 2700 smaller images, with 1350 chosen for training and the remaining 1350 selected for testing.

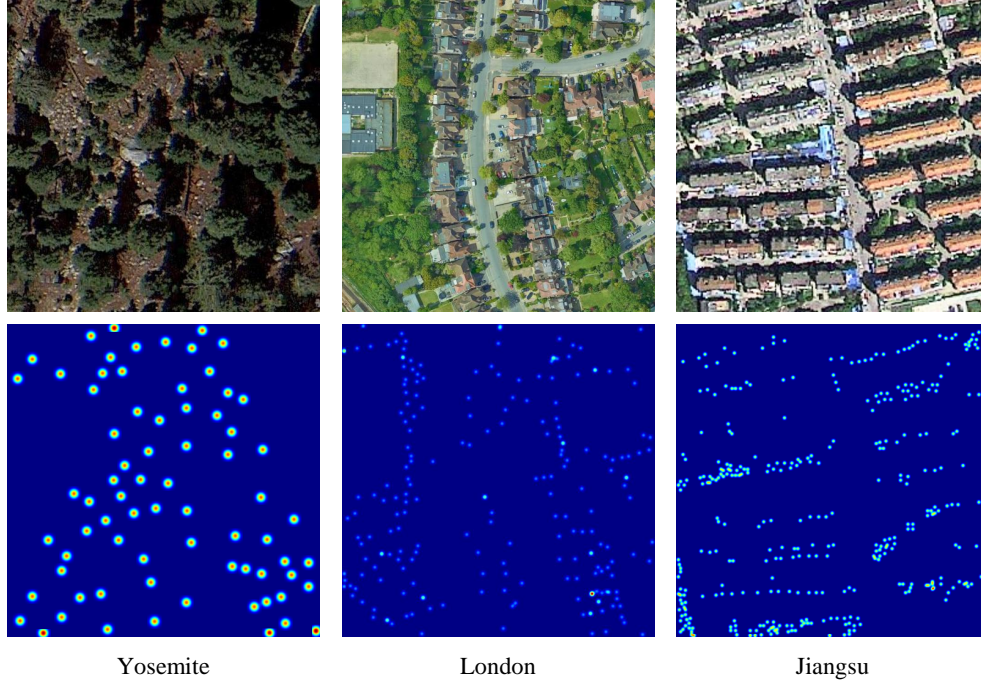


Figure 3: One sample of RGB input image and corresponding tree density map of the Yosemite, London, and Jiangsu datasets.

4.2 Evaluation Metrics

The estimated tree density maps are evaluated using two types of criteria. In the first type, the number of trees in the estimated density map is compared with the reference data using three metrics including mean absolute error (E_{MAE}), root mean squared error (E_{RMS}), and R-Squared (E_{R2}) (Yao et al. (2021); Chen and Shang (2022)). They are defined as follows:

$$E_{MAE} = \frac{1}{N} \sum_{i=0}^N |y_i^{es} - y_i^{gt}| \quad (11)$$

$$E_{RMS} = \sqrt{\frac{1}{N} \sum_{i=0}^N (y_i^{es} - y_i^{gt})^2} \quad (12)$$

$$E_{R^2} = 1 - \frac{\sum_{i=0}^N (y_i^{es} - y_i^{gt})^2}{\sum_{i=0}^N (y_i^{es} - \bar{y}^{gt})^2} \quad (13)$$

where y_i^{es} represents the estimated tree number for the i -th image, y_{gt}^i is the corresponding ground truth tree number. The \bar{y}^{gt} is the mean ground truth tree number over images and N denotes the number of images. In general, higher E_{R2} and lower E_{RMS} and E_{MAE} values indicate better performance.

In the second type, the location of detected trees is assessed using reference data by three metrics including the Precision (E_P), Recall (E_R), and F1-measure (E_{F1}) (Wang et al. (2020b)). They are calculated based

on the number of true positives, false positives, and false negatives obtained from the comparison between the predicted density map and the ground truth density map. Following (Wang et al. (2020b); Liu et al. (2019)), for each point, a search circle with a radius of 15 pixels is considered as the assumed covered area by a tree crown, and the following parameters are computed based on the search circle:

- True Positives (TP): This refers to the number of trees that have been correctly detected. A correctly detected tree is defined as the closest detected tree within the search circle of each ground truth (GT) point.
- False Positives (FP): This represents the number of trees that have been incorrectly detected. Any detected tree that does not fall within the search circle of any ground truth point is considered an incorrect detection.
- False Negatives (FN): This indicates the number of trees that have been missed in detection. When no trees are found within the specified search circle of a given ground truth point, it is considered a missed detection.

The E_P , E_R , and E_{F1} are defined following (Wang et al. (2020b)):

$$E_p = TP / (FP + TP) \tag{14}$$

$$E_R = TP / (FN + TP) \tag{15}$$

$$E_{F1} = 2(E_p \times E_R) / (E_p + E_R) \tag{16}$$

In general, higher E_P , E_R and E_{F1} values indicate better performance.

4.3 Implementation Details

The parameters of the transformer are set according to (Liu et al. (2021b)). To enhance the training set, we apply horizontal flipping and random cropping to source and target domain images (Amirkolaei and Arefi (2019)). Additionally, the input images are randomly cropped to a fixed size of 256×256 for network input. We only select 5 labeled images (5-shot) from the target domain to evaluate the cross-domain capability of AdaTreeFormer by default. The number of batch size, epochs, weight decay, and learning rate are set to 8, 200, 10^{-5} and 10^{-4} , respectively. We use the Adam optimizer. To optimize the adversarial loss function (L_{Adv}), we use a standard stochastic gradient descent method. Initially, we set λ to 0.1 and increase it to 1 after 100 epochs when tree density generator Φ_G starts producing satisfactory tree density maps. As the London dataset images possess high spatial resolution and encompass diverse areas with varying types and densities of tree cover, all parameters are tuned on the London dataset and applied to all experiments. The ground truth consists of the coordinates of tree locations, indicated by annotation dots. We generate the ground truth density maps from the tree locations using Gaussian functions following (Zhang et al. (2016)).

4.4 Comparisons with state of the art

The performance of the proposed AdaTreeFormer is investigated in six different scenarios, considering the study areas of London (S_L), Jiangsu (S_J), and Yosemite (S_Y). In each scenario, one dataset is set as the source domain, and the other as the target domain. For example, in $S_L \rightarrow S_J$, all images of the S_L along with 5 shots of images of S_J are considered for training the network.

In order to compare to other existing methods, the results of different networks are presented in Table 1. AdaCrowd (Reddy et al. (2021)), CODA (Li et al. (2019)), CycleGAN (Zhu et al. (2017a)), SE-CycleGAN (Wang et al. (2004)), and DGCC (Du et al. (2023)) utilize unsupervised domain adaptation techniques where the entire unlabeled images (the whole training set) of the target domain are used for adaptation, while the NLT (Wang et al. (2021b)) and FSCC (Reddy et al. (2020)) employ few shots (5 shots by default) of the target domain with their labels for domain adaptation. Moreover, AdaTreeFormer can be degraded with one subnet for training on the source data only, which is indicated as the Baseline in the table; this trained baseline can be further fine-tuned using 5 shots of the target domain (Baseline+FT). In addition,

the performance of CHSNet (Dai et al. (2023)) and FusionCount (Yiming et al. (2022)) as conventional supervised methods are also fine-tuned using 5 shots in the target domain.

The AdaCrowd (Reddy et al. (2021)) employs a guiding network to predict batch normalization parameters using the target domain images. The CODA (Li et al. (2019)) employs an adversarial learning approach with pyramid patches of multi-scales from both source and target domains. A common approach for achieving suitable results in the target domain is to use unpaired image translation networks. To this end, we use the CycleGAN (Zhu et al. (2017a)) to translate the images of the source domain into the target domain and then use the translated images to estimate tree density maps. In the SE-CycleGAN (Wang et al. (2019a)), the structural similarity index measure (Wang et al. (2004)) is used as an additional cycle loss to improve the translation performance. In DGCC (Du et al. (2023)) a dynamic sub-domain division scheme is suggested for meta-learning in domain generalization and crowd memory modules are utilized to separate domain-specific and domain-invariant image features. FSCC (Reddy et al. (2020)) employs meta-learning to alleviate the domain shift and NLT (Wang et al. (2021b)) models the domain shift at the parameter level using a few shots of the target domain.

Table 1 shows that our AdaTreeFormer significantly outperforms other methods. For instance, in the $S_L \rightarrow S_Y$, we observe a decrease of 4.4 and 3.8 for E_{MAE} and E_{RMS} and an increase of 0.1, 9.0%, 5.0% and 7.2% for E_{R^2} , E_P , E_R , and E_{F1} respectively, when comparing between the previously well-performed NLT and our AdaTreeFomer. In the $S_J \rightarrow S_L$ scenario, our model also has a 4.4 and 2.4 decreases of E_{MAE} and E_{RMS} and an increase of 0.1, 9.7%, 4.7%, and 11.7% for E_{R^2} , E_P , E_R , and E_{F1} compared to NLT, respectively. A similar observation also goes for the other domain adaptation scenarios.

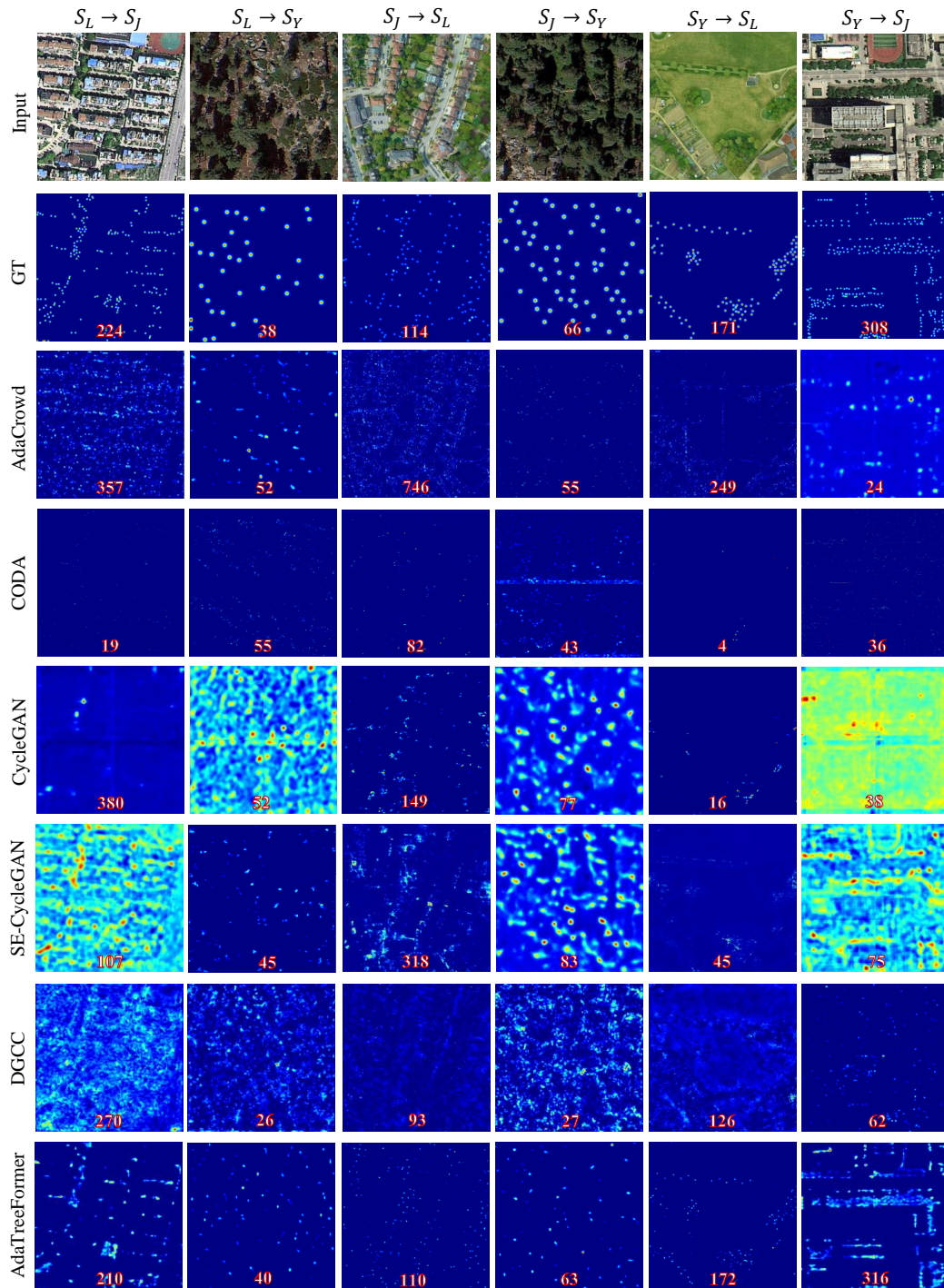


Figure 4: Qualitative results of AdaTreeFormer compared with the state of the art methods including CHSNet+FT, FusionCount+FT, Baseline, Baseline+FT, NLT, FCSS and AdaTreeFormer on KCL-London, Jiangsu, and Yosemite datasets. The first row shows sample images of three utilized datasets. The remaining rows show density maps of GT and other methods.

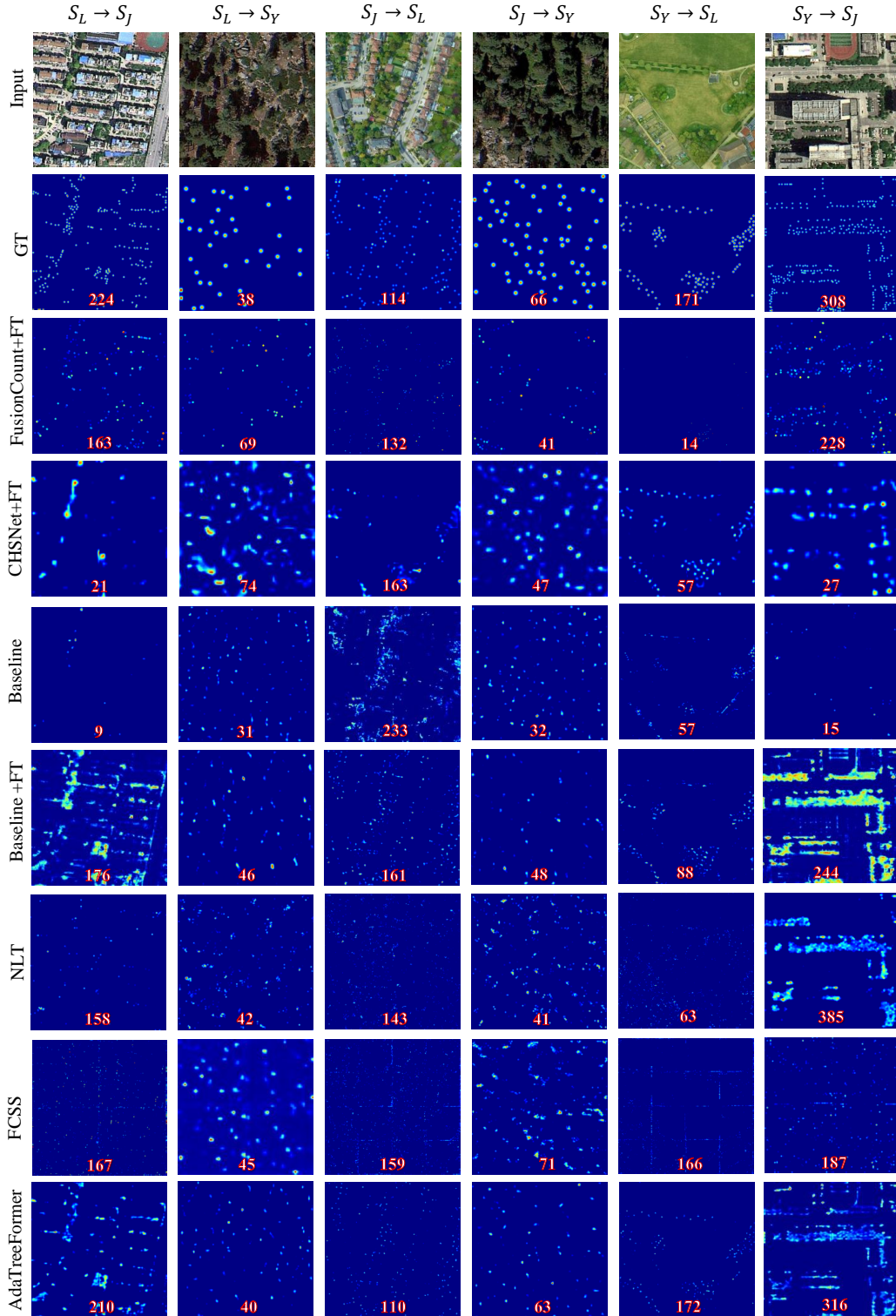


Figure 5: Qualitative results of AdaTreeFormer compared with the state of the arts including AdaCrowd, CODA, CycleGAN, SE-CycleGAN, NLT, FCSS, Baseline, Baseline+FT, and AdaTreeFormer on KCL-London, Jiangsu, and Yosemite datasets. The first row shows sample images of three utilized datasets. The remaining rows show density maps of GT and other methods.

Table 1: Comparison with the state of the art on the London, Jiangsu, and Yosemite datasets. The best and second results are marked in red and blue, respectively.

			$E_{MAE} \downarrow$	$E_{RMS} \downarrow$	$E_{R^2} \uparrow$	$E_P \uparrow$	$E_R \uparrow$	$E_{F1} \uparrow$	$E_{MAE} \downarrow$	$E_{RMS} \downarrow$	$E_{R^2} \uparrow$	$E_P \uparrow$	$E_R \uparrow$	$E_{F1} \uparrow$
Method	Adpt	FS	$S_L \rightarrow S_J$						$S_L \rightarrow S_Y$					
AdaCrowd	✓	✗	243.6	399.6	-0.5	5.6	12.0	7.6	26.1	49.9	-0.6	20.4	15.3	17.5
CODA	✓	✗	239.3	359.6	-0.3	41.9	1.6	3.2	24.7	32.5	-0.1	32.5	23.9	27.6
CycleGAN	✓	✗	284.2	468.5	-1.1	32.8	2.6	4.9	28.9	36.3	-0.6	22.3	24.1	23.2
SE-CycleGAN	✓	✗	268.3	432.5	-1.0	24.6	4.1	7.1	21.8	26.5	0.1	38.4	23.6	29.2
DGCC	✓	✗	192.4	350.4	-0.1	24.5	18.3	21.0	17.4	21.2	0.03	24.2	19.4	21.5
NLT	✓	✓	137.0	194.5	0.4	58.1	39.5	47.0	12.1	14.6	0.6	55.3	63.7	59.2
FSCC	✓	✓	176.1	356.2	-0.2	18.3	25.4	21.3	16.3	19.4	0.4	39.5	31.4	35.0
FusionCount+FT	✗	✓	145.8	203.2	0.4	65.1	14.3	23.5	14.3	18.7	0.4	11.2	47.7	18.1
CHSNet+FT	✗	✓	266.1	414.1	-0.6	96.9	0.2	0.4	22.1	25.6	0.1	58.3	8.0	14.1
Baseline	✗	✗	273.0	421.6	-0.6	43.9	2.7	5.2	25.7	29.8	0.01	35.7	24.1	28.8
Baseline+FT	✗	✓	134.0	181.5	0.5	66.7	33.4	44.5	11.5	15.7	0.6	52.3	61.8	56.7
AdaTreeFormer	✓	✓	122.5	168.4	0.7	75.4	41.8	53.8	7.7	10.8	0.7	64.3	68.7	66.4
			$S_J \rightarrow S_L$						$S_J \rightarrow S_Y$					
AdaCrowd	✓	✗	110.2	143.9	-4.4	33.1	46.3	38.6	26.8	34.5	-0.1	22.7	25.3	24.0
CODA	✓	✗	86.6	103.9	-1.4	38.5	14.6	21.2	22.7	29.4	0.1	35.4	27.1	30.7
CycleGAN	✓	✗	123.6	146.3	-7.5	32.5	42.7	36.9	29.2	36.1	-0.5	29.5	30.6	30.1
SE-CycleGAN	✓	✗	105.8	126.4	-2.5	38.6	43.2	40.8	23.5	28.7	-0.1	35.2	32.7	33.9
DGCC	✓	✗	50.7	63.0	0.04	32.5	21.4	25.8	19.4	24.0	0.1	10.3	23.9	14.4
NLT	✓	✓	25.8	30.7	0.5	61.4	58.3	59.8	11.4	14.9	0.6	59.6	58.2	58.7
FSCC	✓	✓	28.1	33.6	0.5	58.3	53.1	55.6	12.2	18.3	0.4	59.6	67.4	63.2
FusionCount+FT	✗	✓	36.3	59.1	0.01	55.2	2.4	4.6	13.2	16.4	0.5	32.3	45.2	37.7
CHSNet+FT	✗	✓	30.1	40.2	0.2	50.9	14.8	23.0	12.9	15.6	0.6	48.0	23.4	31.5
Baseline	✗	✗	124.7	165.5	0.1	30.7	45.3	36.6	27.4	32.5	-0.2	31.4	22.6	25.5
Baseline+FT	✗	✓	29.4	36.3	0.4	56.7	59.6	58.1	13.5	16.4	0.5	56.2	49.6	52.7
AdaTreeFormer	✓	✓	21.4	28.3	0.6	71.1	72.0	71.5	8.9	11.1	0.7	61.9	69.5	65.5
			$S_Y \rightarrow S_L$						$S_Y \rightarrow S_J$					
AdaCrowd	✓	✗	129.4	142.4	-4.2	35.6	10.4	16.2	182.7	224.5	0.2	43.2	24.5	31.3
CODA	✓	✗	105.3	124.8	-2.3	33.2	12.4	18.1	214.8	334.4	0.02	36.4	19.4	25.1
CycleGAN	✓	✗	134.5	152.7	-8.3	30.1	9.72	14.9	242.8	372.4	-0.01	29.2	15.3	20.1
SE-CycleGAN	✓	✗	112.8	125.6	-3.5	34.6	12.8	18.7	224.9	410.5	-0.1	28.4	18.3	22.3
DGCC	✓	✗	62.5	76.1	-0.6	43.6	37.2	20.0	214.6	372.4	0.04	12.5	19.3	15.2
NLT	✓	✓	34.2	41.6	0.2	60.4	64.1	62.2	143.5	205.2	0.49	62.1	25.4	36.1
FSCC	✓	✓	36.5	42.2	0.2	61.2	59.2	60.3	163.2	197.6	0.5	63.7	22.4	33.2
FusionCount+FT	✗	✓	56.3	68.4	0.02	42.4	10.6	16.9	138.7	239.0	0.5	58.2	14.5	23.2
CHSNet+FT	✗	✓	33.2	56.7	1.3	69.0	4.1	7.7	216.4	382.9	-0.3	22.9	0.5	1.0
Baseline	✗	✗	122.6	129.8	-6.8	39.0	9.5	15.3	271.4	422.1	-0.7	50.0	2.4	4.7
Baseline+FT	✗	✓	34.5	39.3	0.2	58.4	60.2	59.3	149.4	197.3	0.5	69.2	27.4	39.3
AdaTreeFormer	✓	✓	23.1	31.0	0.5	69.3	72.4	70.8	122.8	170.3	0.6	77.5	33.6	46.9

In general, when the target area is Yosemite, the results obtained are more accurate and contain fewer errors. We believe this is because Yosemite covers regions with simpler structures than Jiangsu and London. Consequently, training the network with a large number of these regions and only a few shots of the Yosemite dataset can lead to accurate results. On the other hand, Jiangsu includes different tree types with low and high densities in different landscapes. This factor reduces the results' accuracy when the Jiangsu region is used as a target area.

According to the table, methods that fall within unsupervised domain adaptation do not perform well in the target domains (AdaCrowd, CODA, CycleGAN, SE-CycleGAN, and DGCC). Furthermore, methods that employ a few images related to the target domain for simple fine-tuning also fail to achieve the desired accuracy in their results (FusionCount+FT and CHSNet+FT). Whereas methods that use both adaptation techniques and a few shots of the target domain simultaneously perform better and achieve more accurate results (NLT and FSCC). Moreover, since the domain shift is generally high and only using image translation algorithms (CycleGAN and SE-CycleGAN), subdomain division (GSCC), parameter tuning (AdaCrowd), or

self-supervised loss (CODA) do not achieve good performance in the target domain.

In Figure 4, we present qualitative results of our method compared to other methods that exclusively rely on adaptation techniques. It is evident that our approach outperforms these methods in terms of quality and accuracy. Additionally, in Figure 5, we showcase the results of methods that incorporate only a few shots from the target domain during the training process. Our method demonstrates superior performance in this regard.

4.5 Ablation Study

We analyze AdaTreeFormer in the $S_L \rightarrow S_J$, $S_J \rightarrow S_L$, and $S_Y \rightarrow S_L$ domain adaptation scenarios by ablating its proposed components to evaluate their effects on the model accuracy. We employ the E_{MAE} and E_{F1} for evaluation

4.5.1 Analysis on model architecture

In this section, we investigate the proposed multi-scale feature extraction and attention-to-adapt mechanism.

Efficiency of Data Augmentation. To analyze the performance of the AdaTreeFormer using the Cutmix as data augmentation for the target domain, the accuracy of the achieved results without using the Cutmix is computed (w/o Cutmix) which increases E_{MAE} by 2.8, 2.5, and 2.2 and decreases E_{F1} by 2.6%, 2.7% and 4.4% for the mentioned scenarios in Table 2. Moreover, we can apply Mixup (w/ Mixup) (Zhang et al. (2017a)) or multi-size cropping (Van Gansbeke et al. (2021)) instead of Cutmix to increase the number of training images. In multi-size cropping, the input image undergoes random cropping with different resolutions, and the outcomes are subsequently resized to 256×256 . Accordingly, replacing Cutmix with other ways has reduced the accuracy of the results.

Hierarchical Tree Feature Extraction: The hierarchical structure of the HTFE can be downgraded by reducing the number of scales of the encoder from 4 into 2 (Scales 1 and 2 in Fig. 2) so that only one scale is produced for the decoder (single scale). This scale reduction increases E_{MAE} by 25.7, 6.9, and 7.4 and decreases E_{F1} by 4.6%, 13.1% and 15.2% for $S_L \rightarrow S_J$, $S_J \rightarrow S_L$, and $S_Y \rightarrow S_L$, respectively (Table 2).

Table 2: Ablation study of the employed feature extraction and data augmentation on the $S_L \rightarrow S_J$, $S_J \rightarrow S_L$, and $S_Y \rightarrow S_L$ domain adaptation scenarios.

Scenario	$S_L \rightarrow S_J$		$S_J \rightarrow S_L$		$S_Y \rightarrow S_L$	
Method	E_{MAE}	E_{F1}	E_{MAE}	E_{F1}	E_{MAE}	E_{F1}
Single scale	148.2	49.2	28.3	58.4	30.5	55.6
w/o Cutmix	125.3	51.2	23.9	68.8	25.3	66.4
w/ Crop	127.4	50.8	24.3	67.2	27.8	63.7
w/ Mixup	152.3	24.9	33.4	26.3	36.9	44.8
AdaTreeFormer	122.5	53.8	21.4	71.5	23.1	70.8

Attention-to-adapt mechanism: According to Section 3.2.2, we introduce an attention-to-adapt mechanism. To better evaluate the performance of it, other possible structures are investigated as comparisons.

Source-target subnet. In order to evaluate the efficacy of this subnet, two additional structures are explored (Table 3). In the first structure, no source-target subnet is considered, and only source and target subnets are used for training (Simple-DA). This variant increases E_{MAE} by 14.4 and reduces the E_{F1} by 14.6% across the three mentioned scenarios compared to AdaTreeFormer. In the second structure, a bidirectional source-target and target-source scheme are employed in the source-target subnet (Bi-DA). Using a bidirectional cross-domain attention, the results are improved compared to Simple-DA, but the performance is lower than that of AdaTreeFormer which has a unidirectional cross-domain attention (see Section 3.2.2). Since only a limited number of training images are available in the target domain, it is not appropriate to use

Table 3: Ablation study of the attention-to-adapt mechanism on the $S_L \rightarrow S_J$, $S_J \rightarrow S_L$, and $S_Y \rightarrow S_L$ domain adaptation scenarios.

Scenario	$S_L \rightarrow S_J$		$S_J \rightarrow S_L$		$S_Y \rightarrow S_L$	
Method	E_{MAE}	E_{F1}	E_{MAE}	E_{F1}	E_{MAE}	E_{F1}
Simple-DA	148.4	40.8	29.9	57.8	31.9	53.5
Bi-DA	132.9	44.6	24.7	58.1	25.7	55.3
AdaTreeFormer	122.5	53.8	21.4	71.5	23.1	70.8

Table 4: Ablation study of the DAB on the $S_L \rightarrow S_J$, $S_J \rightarrow S_L$, and $S_Y \rightarrow S_L$ domain adaptation scenarios.

Scale			$S_L \rightarrow S_J$		$S_J \rightarrow S_L$		$S_Y \rightarrow S_L$	
$\frac{1}{8}$	$\frac{1}{16}$	$\frac{1}{32}$	E_{MAE}	E_{F1}	E_{MAE}	E_{F1}	E_{MAE}	E_{F1}
		✓	150.6	41.2	32.2	47.1	37.2	42.6
	✓		137.2	50.7	28.8	62.8	29.9	63.1
✓			142.5	47.3	27.4	60.4	28.3	64.9
✓		✓	128.3	49.2	25.4	62.4	26.9	65.2
	✓	✓	130.8	46.2	24.3	62.3	27.1	67.3
✓	✓		125.3	51.9	23.4	66.3	24.7	65.2
✓	✓	✓	122.5	53.8	21.4	71.5	23.1	70.8

a bidirectional structure for cross-domain attention. In fact, more attention should be paid to the target domain during training as does AdaTreeFormer.

Hierarchical domain attention. We employ the introduced domain attention block (DAB) in a hierarchical way at three scales (*i.e.* $\frac{1}{8}$, $\frac{1}{16}$ and $\frac{1}{32}$) of the proposed framework (Section 3.2.2). To empirically assess the influence of hierarchical domain attention, we perform experiments to analyze the impact of applying the proposed DAB at varying scales. In this regard, when the DAB is applied only at the coarse scale of the decoder ($\frac{1}{32}$), it leads to an increase of 28.1, 10.8, and 14.1 in E_{MAE} and a decrease of 12.6%, 24.4%, 28.2% in E_{F1} for the $S_L \rightarrow S_J$, $S_J \rightarrow S_L$, and $S_Y \rightarrow S_L$ scenarios (Table 4). This decrease in accuracy and increase in error is less when DAB is applied in the $\frac{1}{8}$ and $\frac{1}{4}$ scales. However, the accuracy achieved by applying the DAB at two scales is still lower than when applying it at all three scales of the decoder. For instance, by employing DAB at both $\frac{1}{32}$ and $\frac{1}{16}$ scales, the E_{MAE} increases by 8.3, 2.9, and 4.0, while the E_{F1} decreases by 7.6%, 9.2%, and 3.5% in the mentioned scenarios, in comparison to AdaTreeFormer.

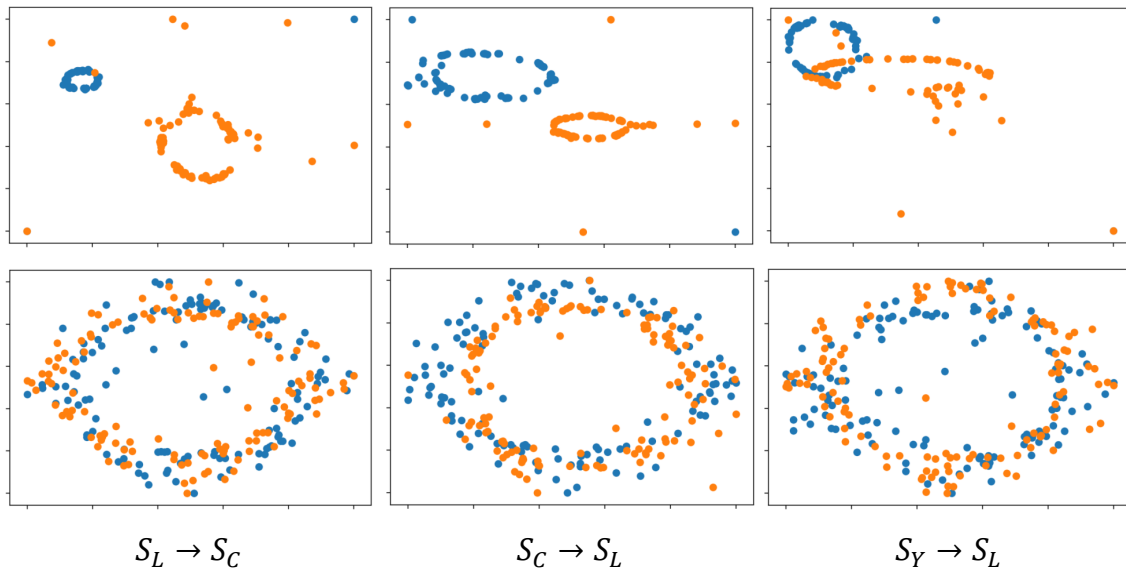


Figure 6: t-SNE visualization of extracted features of the source (blue) and target (orange) domain images through the HTFE (top row) and after applying the cross-domain attention (bottom row).

t-SNE Visualization. The primary objective of domain adaptation is to ensure that the feature distributions obtained from various domains are similar. In this section, we employed t-SNE to reduce the dimensionality of the feature map output through the feature extraction network, as depicted in Fig. 6, to evaluate the effectiveness of the proposed domain adaptation method. The orange circles represent the outcomes obtained from the source domain, while the red circles represent those obtained from the target domain in different tasks. It is evident that in the absence of domain adaptation, the model extracts feature distributions that are farther apart. This suggests that the model extracts distinct features from the source and target domains, making it challenging to produce accurate results. However, after implementing the proposed attention-to-adapt mechanism, the model can extract similar feature distributions from two different domains, enhancing its ability to obtain domain-invariant features from the target domain.

4.5.2 Analysis on training loss

In this section, we investigate the effectiveness of each component of the employed training loss. In order to verify the effectiveness of the training loss, firstly, we use the L_2 loss instead of the L_{TDM} loss (w/ L_2). Table 5 shows that using L_2 increases the E_{MAE} by 78.9, 13.9, and 15.2 for $S_L \rightarrow S_J$, $S_J \rightarrow S_L$, and $S_Y \rightarrow S_L$, respectively. Also, the E_{F1} exhibits a reduction of 25.4%, 48.1%, and 49.5%, respectively. The E_{F1} evaluates a model’s precision and recall in correctly identifying the location of objects within an image, providing a comprehensive measure of its localization performance.

Next, we analyze the performance of the proposed AdaTreeFormer without hierarchical cross domain feature alignment (L_{HCDF_A}), as discussed in Section 3.3.2, denoted as “w/o L_{HCDF_A} ”, which increases E_{MAE} by 2.5 and decreases E_{F1} by 2.7%.

Also, computing the L_{HCDF_A} only on the third scale of the decoder (Single L_{HCDF_A}) instead of three scales of the decoder (Fig. 1) decreases the accuracy compared to the AdaTreeFormer. At last, the performance of the AdaTreeFormer without using adversarial learning is assessed (w/o L_{Adv}). Not using the adversarial learning averagely increases the E_{MAE} by 2.6 and decreases E_{F1} by 2.9%.

Table 5: Ablation study of the employed training loss on the $S_L \rightarrow S_J$, $S_J \rightarrow S_L$, and $S_Y \rightarrow S_L$ domain adaptation scenarios.

Scenario	$S_L \rightarrow S_J$		$S_J \rightarrow S_L$		$S_Y \rightarrow S_L$	
Method	E_{MAE}	E_{F1}	E_{MAE}	E_{F1}	E_{MAE}	E_{F1}
w/ $L2$	201.4	28.4	35.3	23.4	38.3	21.3
w/o $L_{HCDF A}$	126.5	50.4	22.8	69.4	25.3	68.1
Single $L_{HCDF A}$	124.3	52.2	22.0	70.3	24.7	69.3
w/o L_{Adv}	125.8	50.3	23.5	70.2	26.3	66.9
AdaTreeFormer	122.5	53.8	21.4	71.5	23.1	70.8

Table 6: Ablation study of the HCDF A loss on the $S_L \rightarrow S_J$, $S_J \rightarrow S_L$, and $S_Y \rightarrow S_L$ domain adaptation scenarios.

Scenario	$S_L \rightarrow S_J$		$S_J \rightarrow S_L$		$S_Y \rightarrow S_L$	
Method	E_{MAE}	E_{F1}	E_{MAE}	E_{F1}	E_{MAE}	E_{F1}
$\beta_1 = 0.9, \beta_2 = 0.1$	140.5	50.0	26.7	60.2	28.4	59.1
$\beta_1 = 0.7, \beta_2 = 0.3$	132.8	51.2	24.4	63.0	26.1	63.1
$\beta_1 = 0.5, \beta_2 = 0.5$	124.5	51.7	22.4	68.8	24.8	67.1
$\beta_1 = 0.3, \beta_2 = 0.7$	122.5	53.8	21.4	71.5	23.1	70.8
$\beta_1 = 0.1, \beta_2 = 0.9$	123.8	53.2	22.0	71.4	25.3	68.5

Table 7: Ablation study of using 1, 5, and 10-shot labeled data of target domain on the $S_L \rightarrow S_J$, $S_J \rightarrow S_L$, and $S_Y \rightarrow S_L$ domain adaptation scenarios.

Scenario	$S_L \rightarrow S_J$		$S_J \rightarrow S_L$		$S_Y \rightarrow S_L$	
Method	E_{MAE}	E_{F1}	E_{MAE}	E_{F1}	E_{MAE}	E_{F1}
w/o	273.0	5.2	124.7	36.6	122.6	15.5
1 shot	180.2	19.3	56.2	53.1	61.9	48.3
5 shot	122.5	53.8	21.4	71.5	23.1	70.8
10 shot	88.7	60.2	20.1	72.4	22.1	71.6

We specifically investigate the components of $L_{HCDF A}$. In this regard, the impact of different weight values, denoted as β_1 and β_2 , in the $L_{HCDF A}$ loss is investigated. These weight values determine the degree of similarity between the features extracted from the middle subnet and those obtained from the source and target domains. To this end, we change the weight values of β_1 and β_2 from 0.1 to 0.9 with an interval of 0.2 and assess the achieved results (Table 6). According to the results, the network achieves the most accurate results when $\beta_1 = 0.3$ and $\beta_2 = 0.7$.

4.5.3 Analysis on selecting few-shot data

Given that our domain adaptation method necessitates a limited number of labeled images from the target domain, this section will explore the implications of choosing a varying number of few-shot data for AdaTreeFormer. In this regard, 1, 5, and 10 labeled images of the target domain are utilized for training (1, 5, and 10-shot learning) and the results are evaluated. According to Table 7, using 1-shot learning compared to that without adaptation (w/o adaptation) causes decrease in the E_{MAE} by 92.8 and 68.5 and 60.7 and increase in the E_{F1} by 14.1, 16.5 and 32.8, for $S_L \rightarrow S_J$, $S_J \rightarrow S_L$, and $S_Y \rightarrow S_L$, respectively. As the number of employed labeled images from the target domain is raised from 1 to 5 and 10, there is a consistent increase in result accuracy. Employing 10-shot learning instead of 5-shot learning decreases the E_{MAE} by

33.8, 1.3, and 1.0, and increases the E_{F1} by 6.4, 0.9, and 0.8 for the $S_L \rightarrow S_J$, $S_J \rightarrow S_L$, and $S_Y \rightarrow S_L$, respectively.

5 Conclusion

In this paper, we propose a transform-based end-to-end few-shot domain adaptation framework for tree counting from a single high-resolution remote sensing image. In this network, an attention-to-adapt mechanism is introduced to produce robust self- and cross-domain attention maps for tree density estimation using features extracted from the source and target domains. In addition, we proposed a hierarchical cross-domain feature alignment loss to guide the network in extracting robust features from the limited images of the target domain. Adversarial learning is adopted to force the network to reconcile the distribution of source and target domains. The results in domain adaptation scenarios demonstrate that our method outperforms the state of the art.

Acknowledgements

This project (ReSET) has received funding from the European Union’s Horizon 2020 FET Proactive Programme under grant agreement No 101017857. The contents of this publication are the sole responsibility of the ReSET consortium and do not necessarily reflect the opinion of the European Union.

References

- Amini Amirkolaei, H., Shi, M., Mulligan, M., 2023. Treeformer: a semi-supervised transformer-based framework for tree counting from a single high resolution image. arXiv e-prints , arXiv-2307.
- Amirkolaei, H.A., Arefi, H., 2019. Height estimation from single aerial images using a deep convolutional encoder-decoder network. ISPRS journal of photogrammetry and remote sensing 149, 50–66.
- Ammar, A., Koubaa, A., Benjdira, B., 2021. Deep-learning-based automated palm tree counting and geolocation in large farms from aerial geotagged images. Agronomy 11, 1458.
- Arjovsky, M., Chintala, S., Bottou, L., 2017. Wasserstein generative adversarial networks, in: International conference on machine learning, PMLR. pp. 214–223.
- Bart, E., Ullman, S., 2005. Cross-generalization: Learning novel classes from a single example by feature replacement, in: 2005 IEEE Computer Society Conference on Computer Vision and Pattern Recognition (CVPR’05), IEEE. pp. 672–679.
- Chen, G., Shang, Y., 2022. Transformer for tree counting in aerial images. Remote Sensing 14, 476.
- Dai, M., Huang, Z., Gao, J., Shan, H., Zhang, J., 2023. Cross-head supervision for crowd counting with noisy annotations, in: ICASSP 2023-2023 IEEE International Conference on Acoustics, Speech and Signal Processing (ICASSP), IEEE. pp. 1–5.
- Deng, C., Liu, X., Li, C., Tao, D., 2018. Active multi-kernel domain adaptation for hyperspectral image classification. Pattern Recognition 77, 306–315.
- Dosovitskiy, A., Beyer, L., Kolesnikov, A., Weissenborn, D., Zhai, X., Unterthiner, T., Dehghani, M., Minderer, M., Heigold, G., Gelly, S., et al., 2020. An image is worth 16x16 words: Transformers for image recognition at scale. arXiv preprint arXiv:2010.11929 .
- Du, Z., Deng, J., Shi, M., 2023. Domain-general crowd counting in unseen scenarios, in: Proceedings of the AAAI Conference on Artificial Intelligence, pp. 561–570.

- Eisenman, T.S., Churkina, G., Jariwala, S.P., Kumar, P., Lovasi, G.S., Pataki, D.E., Weinberger, K.R., Whitlow, T.H., 2019. Urban trees, air quality, and asthma: An interdisciplinary review. *Landscape and urban planning* 187, 47–59.
- Fei-Fei, L., 2006. Knowledge transfer in learning to recognize visual objects classes, in: *Proceedings of the International Conference on Development and Learning (ICDL)*.
- Fink, M., 2004. Object classification from a single example utilizing class relevance metrics. *Advances in neural information processing systems* 17.
- Finn, C., Abbeel, P., Levine, S., 2017. Model-agnostic meta-learning for fast adaptation of deep networks, in: *International conference on machine learning*, PMLR. pp. 1126–1135.
- Ghanbari Parmehr, E., Amati, M., 2021. Individual tree canopy parameters estimation using uav-based photogrammetric and lidar point clouds in an urban park. *Remote Sensing* 13, 2062.
- Girshick, R., 2015. Fast r-cnn, in: *Proceedings of the IEEE international conference on computer vision*, pp. 1440–1448.
- Han, T., Gao, J., Yuan, Y., Wang, Q., 2020. Focus on semantic consistency for cross-domain crowd understanding, in: *ICASSP 2020-2020 IEEE International Conference on Acoustics, Speech and Signal Processing (ICASSP)*, IEEE. pp. 1848–1852.
- Hennigar, C.R., MacLean, D.A., Amos-Binks, L.J., 2008. A novel approach to optimize management strategies for carbon stored in both forests and wood products. *Forest Ecology and Management* 256, 786–797.
- Hossain, M.A., Kumar, M., Hosseinzadeh, M., Chanda, O., Wang, Y., 2019. One-shot scene-specific crowd counting., in: *BMVC*, p. 217.
- Huang, J., Wu, B., Li, P., Li, X., Wang, J., 2022. Few-shot learning for radar emitter signal recognition based on improved prototypical network. *Remote Sensing* 14, 1681.
- Johnson, M.L., Campbell, L.K., Svendsen, E.S., Silva, P., 2018. Why count trees? volunteer motivations and experiences with tree monitoring in new york city. *Arboriculture & Urban Forestry* 44, 59–72.
- Lassalle, G., Ferreira, M.P., La Rosa, L.E.C., de Souza Filho, C.R., 2022. Deep learning-based individual tree crown delineation in mangrove forests using very-high-resolution satellite imagery. *ISPRS Journal of Photogrammetry and Remote Sensing* 189, 220–235.
- LeCun, Y., Bengio, Y., Hinton, G., 2015. Deep learning. *nature* 521, 436–444.
- Li, W., Yongbo, L., Xiangyang, X., 2019. Coda: Counting objects via scale-aware adversarial density adaption, in: *2019 IEEE International Conference on Multimedia and Expo (ICME)*, IEEE. pp. 193–198.
- Liu, G., Wang, T., Zhang, S., He, K., 2022a. Generating pseudo-labels adaptively for few-shot model-agnostic meta-learning. *arXiv preprint arXiv:2207.04217* .
- Liu, J., Shen, J., Zhao, R., Xu, S., 2013. Extraction of individual tree crowns from airborne lidar data in human settlements. *Mathematical and Computer Modelling* 58, 524–535.
- Liu, T., Yao, L., Qin, J., Lu, J., Lu, N., Zhou, C., 2021a. A deep neural network for the estimation of tree density based on high-spatial resolution image. *IEEE Transactions on Geoscience and Remote Sensing* 60, 1–11.
- Liu, Y., Li, X., 2014. Domain adaptation for land use classification: A spatio-temporal knowledge reusing method. *ISPRS journal of photogrammetry and remote sensing* 98, 133–144.
- Liu, Y., Shi, M., Zhao, Q., Wang, X., 2019. Point in, box out: Beyond counting persons in crowds, in: *Proceedings of the IEEE/CVF Conference on Computer Vision and Pattern Recognition*, pp. 6469–6478.

- Liu, Y., Wang, Z., Shi, M., Satoh, S., Zhao, Q., Yang, H., 2022b. Discovering regression-detection bi-knowledge transfer for unsupervised cross-domain crowd counting. *Neurocomputing* 494, 418–431.
- Liu, Z., Lin, Y., Cao, Y., Hu, H., Wei, Y., Zhang, Z., Lin, S., Guo, B., 2021b. Swin transformer: Hierarchical vision transformer using shifted windows, in: *Proceedings of the IEEE/CVF international conference on computer vision*, pp. 10012–10022.
- Machefer, M., Lemarchand, F., Bonnefond, V., Hitchins, A., Sidiropoulos, P., 2020. Mask r-cnn refitting strategy for plant counting and sizing in uav imagery. *Remote Sensing* 12, 3015.
- Mishra, N., Rohaninejad, M., Chen, X., Abbeel, P., 2017. A simple neural attentive meta-learner. *arXiv preprint arXiv:1707.03141* .
- Ong, W.J., Ellison, J.C., 2021. A framework for the quantitative assessment of mangrove resilience, in: *Dynamic Sedimentary Environments of Mangrove Coasts*. Elsevier, pp. 513–538.
- Oscó, L.P., De Arruda, M.d.S., Junior, J.M., Da Silva, N.B., Ramos, A.P.M., Moryia, É.A.S., Imai, N.N., Pereira, D.R., Creste, J.E., Matsubara, E.T., et al., 2020. A convolutional neural network approach for counting and geolocating citrus-trees in uav multispectral imagery. *ISPRS Journal of Photogrammetry and Remote Sensing* 160, 97–106.
- Pang, Y., Lin, J., Qin, T., Chen, Z., 2021. Image-to-image translation: Methods and applications. *IEEE Transactions on Multimedia* 24, 3859–3881.
- Ravi, S., Larochelle, H., 2017. Optimization as a model for few-shot learning, in: *International conference on learning representations*.
- Reddy, M.K.K., Hossain, M., Rochan, M., Wang, Y., 2020. Few-shot scene adaptive crowd counting using meta-learning, in: *Proceedings of the IEEE/CVF winter conference on applications of computer vision*, pp. 2814–2823.
- Reddy, M.K.K., Rochan, M., Lu, Y., Wang, Y., 2021. Adacrowd: Unlabeled scene adaptation for crowd counting. *IEEE Transactions on Multimedia* 24, 1008–1019.
- Redmon, J., Divvala, S., Girshick, R., Farhadi, A., 2016. You only look once: Unified, real-time object detection, in: *Proceedings of the IEEE conference on computer vision and pattern recognition*, pp. 779–788.
- Ren, S., He, K., Girshick, R., Sun, J., 2015. Faster r-cnn: Towards real-time object detection with region proposal networks. *Advances in neural information processing systems* 28.
- Santoro, A., Bartunov, S., Botvinick, M., Wierstra, D., Lillicrap, T., 2016. Meta-learning with memory-augmented neural networks, in: *International conference on machine learning*, PMLR. pp. 1842–1850.
- dos Santos Ferreira, A., Freitas, D.M., da Silva, G.G., Pistori, H., Folhes, M.T., 2019. Unsupervised deep learning and semi-automatic data labeling in weed discrimination. *Computers and Electronics in Agriculture* 165, 104963.
- Simonyan, K., Zisserman, A., 2014. Very deep convolutional networks for large-scale image recognition. *arXiv preprint arXiv:1409.1556* .
- van Soesbergen, A., Chu, Z., Shi, M., Mulligan, M., 2022. Dam reservoir extraction from remote sensing imagery using tailored metric learning strategies. *IEEE Transactions on Geoscience and Remote Sensing* 60, 1–14.
- Song, S., Yu, H., Miao, Z., Zhang, Q., Lin, Y., Wang, S., 2019. Domain adaptation for convolutional neural networks-based remote sensing scene classification. *IEEE Geoscience and Remote Sensing Letters* 16, 1324–1328.

- Tuia, D., Persello, C., Bruzzone, L., 2016. Domain adaptation for the classification of remote sensing data: An overview of recent advances. *IEEE geoscience and remote sensing magazine* 4, 41–57.
- Van Gansbeke, W., Vandenhende, S., Georgoulis, S., Gool, L.V., 2021. Revisiting contrastive methods for unsupervised learning of visual representations. *Advances in Neural Information Processing Systems* 34, 16238–16250.
- Vaswani, A., Shazeer, N., Parmar, N., Uszkoreit, J., Jones, L., Gomez, A.N., Kaiser, L., Polosukhin, I., 2017. Attention is all you need. *Advances in neural information processing systems* 30.
- Vinyals, O., Blundell, C., Lillicrap, T., Wierstra, D., et al., 2016. Matching networks for one shot learning. *Advances in neural information processing systems* 29.
- Wang, B., Liu, H., Samaras, D., Nguyen, M.H., 2020a. Distribution matching for crowd counting. *Advances in neural information processing systems* 33, 1595–1607.
- Wang, H., Zhu, Y., Adam, H., Yuille, A., Chen, L.C., 2021a. Max-deeplab: End-to-end panoptic segmentation with mask transformers, in: *Proceedings of the IEEE/CVF conference on computer vision and pattern recognition*, pp. 5463–5474.
- Wang, Q., Gao, J., Lin, W., Li, X., 2020b. Nwpu-crowd: A large-scale benchmark for crowd counting and localization. *IEEE transactions on pattern analysis and machine intelligence* 43, 2141–2149.
- Wang, Q., Gao, J., Lin, W., Yuan, Y., 2019a. Learning from synthetic data for crowd counting in the wild, in: *Proceedings of the IEEE/CVF conference on computer vision and pattern recognition*, pp. 8198–8207.
- Wang, Q., Han, T., Gao, J., Yuan, Y., 2021b. Neuron linear transformation: Modeling the domain shift for crowd counting. *IEEE Transactions on Neural Networks and Learning Systems* 33, 3238–3250.
- Wang, Y., Zhu, X., Wu, B., 2019b. Automatic detection of individual oil palm trees from uav images using hog features and an svm classifier. *International Journal of Remote Sensing* 40, 7356–7370.
- Wang, Z., Bovik, A.C., Sheikh, H.R., Simoncelli, E.P., 2004. Image quality assessment: from error visibility to structural similarity. *IEEE transactions on image processing* 13, 600–612.
- Weinstein, B.G., Marconi, S., Bohlman, S., Zare, A., Singh, A., Graves, S.J., White, E., 2020. Neon crowns: a remote sensing derived dataset of 100 million individual tree crowns. *BioRxiv* .
- Weinstein, B.G., Marconi, S., Bohlman, S., Zare, A., White, E., 2019. Individual tree-crown detection in rgb imagery using semi-supervised deep learning neural networks. *Remote Sensing* 11, 1309.
- Yang, J., Wang, X., Luo, Z., 2024. Few-shot remaining useful life prediction based on meta-learning with deep sparse kernel network. *Information Sciences* 653, 119795.
- Yao, L., Liu, T., Qin, J., Lu, N., Zhou, C., 2021. Tree counting with high spatial-resolution satellite imagery based on deep neural networks. *Ecological Indicators* 125, 107591.
- Yiming, M., Sanchez, V., Guha, T., 2022. Fusioncount: Efficient crowd counting via multiscale feature fusion, in: *Proceedings of the IEEE International Conference on Image Processing, Bordeaux, France*.
- Yun, S., Han, D., Oh, S.J., Chun, S., Choe, J., Yoo, Y., 2019. Cutmix: Regularization strategy to train strong classifiers with localizable features, in: *Proceedings of the IEEE/CVF international conference on computer vision*, pp. 6023–6032.
- Zhang, H., Cisse, M., Dauphin, Y.N., Lopez-Paz, D., 2017a. mixup: Beyond empirical risk minimization. *arXiv preprint arXiv:1710.09412* .
- Zhang, Y., Yang, L., Chen, J., Fredericksen, M., Hughes, D.P., Chen, D.Z., 2017b. Deep adversarial networks for biomedical image segmentation utilizing unannotated images, in: *Medical Image Computing*

- and Computer Assisted Intervention- MICCAI 2017: 20th International Conference, Quebec City, QC, Canada, September 11-13, 2017, Proceedings, Part III 20, Springer. pp. 408–416.
- Zhang, Y., Zhou, D., Chen, S., Gao, S., Ma, Y., 2016. Single-image crowd counting via multi-column convolutional neural network, in: Proceedings of the IEEE conference on computer vision and pattern recognition, pp. 589–597.
- Zheng, J., Fu, H., Li, W., Wu, W., Zhao, Y., Dong, R., Yu, L., 2020. Cross-regional oil palm tree counting and detection via a multi-level attention domain adaptation network. *ISPRS Journal of Photogrammetry and Remote Sensing* 167, 154–177.
- Zhu, J.Y., Park, T., Isola, P., Efros, A.A., 2017a. Unpaired image-to-image translation using cycle-consistent adversarial networks, in: Proceedings of the IEEE international conference on computer vision, pp. 2223–2232.
- Zhu, X.X., Tuia, D., Mou, L., Xia, G.S., Zhang, L., Xu, F., Fraundorfer, F., 2017b. Deep learning in remote sensing: A comprehensive review and list of resources. *IEEE geoscience and remote sensing magazine* 5, 8–36.